

Taking the Pulse of PyroCumulus Clouds

C. K. Gatebe^{1,2}, T. Varnai^{2,3}, R. Poudyal^{2,4}, C. Ichoku² and M. D. King⁵

¹*Universities Space Research Association, Columbia, Maryland 21228, USA.*

²*NASA Goddard Space Flight Center, Greenbelt, Maryland 20771, USA.*

³*University of Maryland, Baltimore County, Baltimore, Maryland 21228*

⁴*Science Systems and Applications, Inc., Lanham, Maryland 20706, USA*

⁵*Laboratory for Atmospheric and Space Physics, University of Colorado, Boulder, Colorado, USA.*

Correspondence: charles.k.gatebe@nasa.gov

Abstract: Forest fires can burn large areas, but can also inject smoke into the upper troposphere/lower stratosphere (UT/LS), where stakes are even higher for climate, because emissions tend to have a longer lifetime, and can produce significant regional and even global climate effects, as is the case with some volcanoes. Large forest fires are now believed to be more common in summer, especially in the boreal regions, where pyrocumulus (pyroCu), and occasionally pyrocumulonimbus (pyroCb) clouds are formed, which can transport emissions into the UT/LS. A major difficulty in developing realistic fire plume models is the lack of observational data within fire plumes that resolves structure at a few 100 m scales, which can be used to validate these models. Here, we report detailed airborne radiation measurements within strong pyroCu taken over boreal forest fires in Saskatchewan, Canada during the Arctic Research of the Composition of the Troposphere from Aircraft and Satellites (ARCTAS)

1 summer field campaign in 2008. We find that the angular distribution of radiance
2 within the pyroCu is closely related to the diffusion domain in water clouds and can
3 be described by very similar simple cosine functions. We demonstrate with Monte
4 Carlo simulations that radiation transport in pyroCu is inherently a 3D phenomenon
5 and must account for particle absorption. However, the simple cosine function prom-
6 ises to offer an easy solution for climate models. The presence of a prominent smoke
7 core, defined by strong extinction in the UV, VIS and NIR, suggests that the core
8 might be an important pathway for emission transport to the upper troposphere and
9 lower stratosphere. We speculate that this plume injection core is generated and sus-
10 tained by complex processes not yet well understood, but not necessarily related di-
11 rectly to the intense fires that originally initiated the plume rise.

12

1 1. Introduction

2 Forest fires are known to burn vast areas, and also inject smoke into the upper tropo-
3 sphere/lower stratosphere (UT/LS), where the stakes are even higher for climate, because
4 emissions tend to have a longer lifetime, and can cause regional and global climate effects,
5 as is the case with some volcanic eruptions. Fires of this nature are common in summer in
6 the boreal regions of Alaska, Canada, and Russia (Fromm et al., 2010; Soja et al., 2007;
7 Stocks et al., 2003).

8 Large forest fires release enough energy, both sensible and latent heat, to lift the
9 smoke-laden air beyond the condensation level, resulting in the formation of cumulus
10 clouds. Due to their association with fires, these clouds are commonly referred to as pyro-
11 cumulus (pyroCu), or pyrocumulonimbus (pyroCb) when convective storms are sufficiently
12 deep to glaciate and form anvils. The pyroCbs have unique dynamical and microphysical
13 structures, and constitute an important mechanism for troposphere-stratosphere transport of
14 biomass burning emissions such as aerosols and trace gases, thereby contributing to raising
15 their budgets in the UT/LS (Damoah et al., 2006; Luderer et al., 2006; Trentmann et al.,
16 2006; Fromm et al., 2005; Fromm and Servranckx, 2003). There is now growing evidence
17 that wildfires should be considered as additional sources of aerosol and trace gases to the
18 UT/LS region, which was previously thought to be primarily dominated by volcanic erup-
19 tions (Fromm et al., 2010; Luderer et al., 2006).

20 There is still significant uncertainty on how much of the energy released by combus-
21 tion contributes to local heating of the atmosphere and is available for convection, and how
22 much of the energy is lost due to radiative processes. Commonly found estimates for the
23 radiative energy are between nearly 14% (Wooster et al., 2005) and 50% (McCarter and
24 Broido, 1965; Packham, 1969). These estimates are based on laboratory studies or observa-
25 tions of small-scale fires, and their application to large-scale crown fires resulting in

1 pyroCu or pyroCb convection is subject to considerable uncertainty. The interaction of this
2 radiative energy with atmospheric constituents is also highly uncertain. In the thermal in-
3 frared, where most of the fire radiation is emitted (Wooster, 2002), aerosols are rather inef-
4 ficient absorbers. It is likely that most of the radiative energy from the fire is absorbed by
5 cloud droplets or gaseous absorption at cloud base or in air masses that are entrained into
6 the convective plume. This implies that the radiative energy from the fire is trapped in the
7 lower part of the pyro-convection and therefore contributes to the convective energy. It is
8 therefore important to consider the radiative processes in detail.

9 A major challenge in developing realistic fire plume models is the lack of observa-
10 tional data within forest fire plumes that can be used for validating these models. This is not
11 a big surprise, because making observations within forest fire plumes is challenging at best,
12 and flying into the “core” of rising smoke can be very risky. The possibility of damaging
13 expensive instrumentation is also high. Here, we report detailed radiation measurements
14 from within a pyroCu core taken onboard the NASA P-3B aircraft during the Arctic Re-
15 search of the Composition of the Troposphere from Aircraft and Satellites (ARCTAS) ex-
16 periment, which took place in Canada in June-July 2008 (Jacob et al., 2010). Such mea-
17 surements are needed in the investigations of pyro-convection on the spatial scale of indi-
18 vidual events, i.e., tens of meters to a few hundred meters. This would contribute to the
19 understanding of the vertical and cross-isentropic transport mechanisms responsible for
20 high-altitude tropospheric and stratospheric injection (Luderer et al., 2006). These radiation
21 measurements are unique; we are not aware of any previous radiation measurements within
22 a forest fire plume at the scales described in the next section.

23 This study focuses on 2 July 2008 and 6 July 2008, the fourth and sixth flights of the
24 P-3B, respectively, out of Cold Lake, Canada during ARCTAS. These flights provided op-
25 portunities for in situ observations of flaming fires, plume evolution and vertical profiles of

1 plumes in homogeneous fire outflow regions. Most importantly, they are the only flights
2 where the P-3B penetrated the pyroCu clouds of active fire plumes. In this study, we em-
3 phasize data obtained with a multi-wavelength scanning radiometer, NASA's Cloud Ab-
4 sorption Radiometer (CAR; Gatebe et al., 2003; King et al., 1986), which provides unpre-
5 cedented detail on pyroCu clouds.

6 The CAR instrument measures scattered light in 14 spectral bands between 0.34 and
7 2.30 μm and has a unique scanning geometry and is able to scan a scene of the atmosphere
8 and surface over a 190° scan angle and at high angular resolution (1° instantaneous field of
9 view). When it is flown inside clouds, it is able to provide a side view in the zenith and na-
10 dir directions, and all scattering angles in between from an aircraft platform with as much
11 as a 5° roll—assuming no aircraft pitch. Data are sampled simultaneously and continuously
12 on nine individual detectors. Eight of the data channels for spectral bands from 0.34 to 1.27
13 μm are always registered during the operation, while the ninth data channel is registered for
14 signal selected among six spectral channels (1.55–2.30 μm) on a filter wheel. The filter
15 wheel can either cycle through all six spectral bands at a prescribed interval (usually chan-
16 ging filter every fifth scan line), or lock onto any one of the six spectral bands, mostly
17 1.656, 2.103, or 2.205 μm , and sample it continuously

18 **2. Observational Assessment of the PyroCu**

19 Some of the biggest Saskatchewan fires during the 2008 summer ARCTAS campaign
20 burned west of McIntosh Lake and east of Lake Athabasca in Canada. On 2 July (P-3 Flight
21 #18/CAR Flight # 2017) and 6 July (P-3 Flight #20/CAR Flight # 2019) the conditions for
22 fires seemed right, as a cold front moved over the region setting up conditions conducive to
23 sending hot smoke plumes billowing into the upper atmosphere. The P-3B aircraft, with its
24 suite of instruments, was in the air and managed to acquire very good fire data. Below, we
25 provide a general description of the 2 July flight and the primary instruments that were op-

erating during the flight. We will not describe the 6 July flight because of similarities between the two flights, however, full details for this flight can be found on the CAR website (http://car.gsfc.nasa.gov/data/index.php?id=115&mis_id=8&n=ARCTAS). Through these descriptions, we attempt to paint a picture of the nature and character of the fires and in addition, create a preamble for further work on pyroCu and their effects on climate.

2.1 General Description of Flight 2017, 2 July 2008

Our objectives for this flight included flying a segment under the Terra satellite, coordinated with the NASA B-200 carrying the High Spectral Resolution Lidar (HSRL) and the Research Scanning Polarimeter (RSP) instrument) with radiation measurements under clear sky conditions stacked at different altitudes, and in situ observations of flaming fires, showing plume evolution and vertical profiles in homogeneous fire outflow regions. The flight took 6 hours and 20 minutes, with take off at 15:31 UTC (9:31 a.m. local time; see flight log: http://car.gsfc.nasa.gov/data/index.php?id=113&mis_id=8&n=ARCTAS). Fig. 1a shows the flight path from Cold Lake, heading northeast towards Reindeer Lake. We made measurements collocated with the B-200 for about 50 minutes beginning at 16:25 UTC, and observed active fires of different intensities under scattered cloud conditions. We penetrated an active fire plume near McIntosh Lake at two altitudes, 1303 m (19:18 UTC) and 294 m (19:49 UTC) above the local surface, and flew along the plume axis for about 80 km to study the evolution of aerosol microphysics during downwind transport. Between the two penetrations, we obtained radiation measurements in a vertical profile in the most homogeneous part of the plume and flew across-plume at a low-level. We also sampled outflow from a pyroCu cloud and penetrated the cloud to sample the inside. Fig. 1b shows an image taken by the Moderate Resolution Imaging Spectroradiometer (MODIS) flying aboard the Aqua satellite at 19:35 UTC over the region highlighted in the white box in Fig. 1a. The cloud fields seen in the satellite image are most likely associated with the active

1 fires in the region. Note that the green squares represent fire locations detected by MODIS
2 on the Terra satellite, taken during the overpass earlier that day, at 17:55 UTC. The red
3 squares represent fire locations based on high radiance, relative to background, as seen with
4 the MODIS/Aqua 4- μm channel during the overpass (e.g. Giglio, 2003).

5 Figs. 1c and 1d show CAR quicklook images selected from a section of the flight
6 where the aircraft went through a pyroCu core during the flight of 2 July (the green line
7 highlights the flight path through the pyroCu, whereas the orange dot in Fig. 1b marks the
8 location of the plume core). A combination of different CAR bands representing red,
9 green, and blue colors helps to differentiate between clouds and smoke and to see through
10 smoke, revealing land surface features such as green vegetation and dark water bodies (see
11 Fig. 1c: false-color RGB(0.47, 0.38, 0.34) μm ; Fig 1d: false-color RGB(1.66, 1.04, 0.38)
12 μm). As shown in Fig. 1d, the fire was widespread, covering hundreds of hectares, and it
13 took the aircraft \sim 15 seconds to cross the core (the core covers a ground area \sim 2 km, where
14 the measured aircraft groundspeed varied between 127 ms^{-1} and 138 ms^{-1}). The aircraft
15 altitude changed dramatically while traversing the core, rising by 93 m, from 2747 m to
16 2840 m above mean sea level, an indication of strong updrafts $>8 \text{ ms}^{-1}$.

17 The height of the 2 July PyroCu top above ground was > 3000 m, and the boundary
18 layer (BL) height at the fire location and time of aircraft data acquisition was 1976 m. The
19 BL was obtained by interpolating the values for 12 noon and 3 pm local times from the
20 NASA Goddard Earth Observing System (GEOS-5) data provided by the Global Modelling
21 and Assimilation Office (GMAO). Therefore, the pyroCu extended well above the boun-
22 dary layer. Recent studies based on digitized plume height analysis from the Multi-angle
23 Imaging SpectroRadiometer (MISR) instrument aboard the Terra satellite have shown that
24 of order 10% of the plumes are injected higher than 0.5 km above the BL; out of eight
25 North American biome types evaluated, fire plumes from boreal forests (which include the

study area) are typically injected the highest, with a median injection top height of ~1200 m (as compared to ~800 m for croplands; Kahn et al., 2008; Val Martin et al., 2010). Those studies also found a correlation between the plume injection height and fire radiative power (FRP) measurements from MODIS (Ichoku et al., 2008), indicating that in addition to atmospheric stability structure, fire intensity (represented by FRP) has a strong influence on plume injection height; plume top heights that reached the free troposphere (FT) were produced mainly by high intensity fires having a median FRP of order 500 MW. Table 1 shows the FRP values of the MODIS fire pixels (depicting their relative intensities) from Aqua coinciding with 2 July 2008 flights (in space but not in time). The FRP data record corresponding spatially to the pyroCu plume penetrated by P-3B is shown in boldface characters. However, because of the large difference in time between the FRP measurement from Aqua-MODIS (19:35 UTC) and P-3B penetration of the pyroCu (~21:05 UTC), this FRP value is much less than what would have been required to generate such a high plume and the associated pyroCu. It is probable that the fire became much stronger by the time of the pyroCu measurement. For the P-3B pyroCu penetration on 6 July 2008, no fire pixels were detected by MODIS within a few km of the pyroCu. It is believed that the pyroCu may have moved substantially away from the fire at the time of its penetration, making it impossible to link it to any specific fire detected by MODIS. Therefore, to establish a cause and effect relationship of such transient features as fires and their associated plumes and pyroCu, it is crucial to conduct airborne measurements in synchronicity with satellite overpasses and ground-based measurements whenever possible.

22 2.2 *NASA P-3B Payload during ARCTAS 2008*

23 Fig. 2a shows the platform we used in this campaign, the NASA P-3B aircraft. The
24 picture was taken at NASA Ames on 24 June 2008 just before a transit flight to Cold Lake,
25 Canada at the start of the ARCTAS summer campaign. The P-3B payload included 10 pri-

1 many instruments (see Table 2) for measuring aerosol optical depth, aerosol extinction and
2 scattering, aerosol size distribution (Russell et al., 1999; Clarke et al., 2007), spectral (0.380
3 – 2.200 μm) and broadband downwelling and upwelling solar (0.2–3.6 μm), and IR irradiance
4 (4.5–42 μm ; Pilewskie et al., 2003; Bucholtz personal communication:
5 <http://airbornescience.nasa.gov/instrument/BBR>), angular distribution of scattered radiation
6 in different directions (Gatebe et al., 2003), cloud condensation nuclei (Roberts and Nenes,
7 2005; Lance et al., 2006), and NO_2 and carbon monoxide (Strawa et al., 2007; Provencal et
8 al. 2005). The base meteorological and navigational measurements were provided by the
9 Project Data System, which is the primary navigational data system for P-3B investigators.

10 Fig. 2b shows a schematic of the CAR instrument (Gatebe et al., 2003; King et al.,
11 1986), highlighting its main features. Fig. 2c shows a pyroCu taken onboard the NASA P-
12 3B on 2 July 2008 near Reindeer Lake, Saskatchewan, Canada. The aircraft flew around
13 these fires, sampling clean air upwind and the polluted air downwind. It then flew through
14 the smoke at various altitudes, probing and charting changes in concentration and the
15 "chemical evolution" of the compounds emitted by the fires. The plane also flew into the
16 "core" of the rising fire plumes, where the CAR instrument managed to acquire good data
17 as discussed in this study. These represent the first such measurements in the core of a
18 pyroCb of which we are aware. (See pictures from the 2 July flight on the CAR website at
19 http://car.gsfc.nasa.gov/data/photos.php?mis_id=8&n=ARCTAS&d=2008-07-02&f=2017&l=h
20 and [from the 6 July flight at
21 \[http://car.gsfc.nasa.gov/data/photos.php?mis_id=8&n=ARCTAS&d=2008-07-06&f=2019&l=h\]\(http://car.gsfc.nasa.gov/data/photos.php?mis_id=8&n=ARCTAS&d=2008-07-06&f=2019&l=h\).](http://car.gsfc.nasa.gov/data/photos.php?mis_id=8&n=ARCTAS&d=2008-07-06&f=2019&l=h)

22 In the next section, we will present an analysis of the CAR measurements inside
23 pyroCu and results from a Monte Carlo simulation of the radiation field within optically
24 dense media analogous to those observed above.

1 **3. Results and Discussion**

2 *3.1 Analysis of CAR Measurements*

3 The core of the pyroCu as seen in Figs. 1c and 1d stands out as a very dark region of
4 the plume, where radiation seems to be uniformly distributed and dominated by strong ab-
5 sorption in all directions. The CAR instrument measured very low spectral radiance values
6 ($< 1 \text{ Wm}^{-2}\mu\text{m}^{-1}\text{sr}^{-1}$ in the ultraviolet and visible bands having $\lambda < 0.5 \mu\text{m}$, and at $\lambda = 1.6$
7 μm , and $2\text{--}5 \text{ Wm}^{-2}\mu\text{m}^{-1}\text{sr}^{-1}$ for bands between $0.5 \mu\text{m}$ and $1.3 \mu\text{m}$), independent of direc-
8 tion. The radiance distributions within the core at two zenith angles: 5° and 175° at 0.472
9 μm , shown in Fig. 3 demonstrate that there is hardly any difference between the downwel-
10 ling and upwelling radiance within the core region. The a, b and c images in this figures
11 were taken by a forward camera aboard the NASA P-3B at the entry, core, and exit points
12 in the pyroCu. Note the brownish color of the plume inside the core region. The radiance
13 decreases by about two orders of magnitude from outside to the central part of the core, ir-
14 respective of the direction and wavelength. We speculate that the core region plays an im-
15 portant role as the main physical pathway through which emissions from fires are trans-
16 ported into the upper troposphere/lower stratosphere (UT/LS), but this observation needs to
17 be validated.

18 Fig. 4 compares relative spectral radiance as a function of zenith angle for internally
19 scattered radiation measured deep inside an optically thick water cloud, pyroCu and a thick
20 “pure” smoke, which is defined by lack of reflectance sensitivity in the near-infrared bands
21 ($\lambda \geq 0.87 \mu\text{m}$), at selected CAR wavelengths. According to King et al. (1990), radiance
22 measurements from an individual scan of the CAR are considered to be in the diffusion
23 domain, if three conditions are satisfied: (i) the zenith radiance exceeds the nadir radiance,
24 (ii) the maximum deviation from the theoretical cosine curve is less than or equal to 5% of
25 the mean amplitude, and (iii) the number of times the deviations from a cosine distribution

1 changes sign is greater than or equal to 4, which helps to assure that fluctuations are ran-
 2 dom, and not systematic drifts. These criteria pertain to the diffusion domain of an optically
 3 thick media if the scattering is conservative (no absorption), and thus are to be expected for
 4 liquid water clouds at wavelengths around 0.67 μm (as seen in Fig. 4a). The theoretical
 5 curve is generated from measured zenith and nadir radiances using the following cosine
 6 relationship

$$I(\tau, \cos \theta) = a + b \cos \theta \quad (1)$$

8 where

$$\begin{aligned} 9 \quad a &= \frac{1}{2}(I_0(\tau, 1) + I_{180}(\tau, -1)), \\ 10 \quad b &= \frac{1}{2}(I_0(\tau, 1) - I_{180}(\tau, -1)) \end{aligned} \quad (1a)$$

11 and I_0 and I_{180} are the zenith and nadir radiances at $\theta = 0^\circ$ and $\theta = 180^\circ$, respectively. From
 12 Eq. 1a, we came up with a general equation for any two downward and upward viewing
 13 angles in the form

$$\begin{aligned} 14 \quad a &= \frac{1}{2}(I_{\theta'}(\tau, \cos \theta') + I_{180-\theta'}(\tau, -\cos \theta')), \\ 15 \quad b &= \frac{1}{2 \cos \theta'}(I_{\theta'}(\tau, \cos \theta') - I_{180-\theta'}(\tau, -\cos \theta')) \end{aligned} \quad (1b)$$

16 As such, Eq. 1b is not restricted to using zenith ($\theta = \theta' = 0^\circ$) and nadir ($\theta = \theta' = 180^\circ$) in-
 17 put radiances, unlike Eq. 1a, and can be used to describe the radiation field in optically
 18 thick media given any two downward and upward viewing directions, or $\theta' = 90^\circ$ (where b
 19 = $I_{90}(\tau)$) and any other direction. This general formula can be applied to CAR observa-
 20 tions away from the zenith and nadir directions, and therefore can accommodate the reali-
 21 ties of data acquisition on an airborne platform that has a nonzero pitch and/or roll angle.

22 For the liquid water cloud case, obtained on 29 June 2008 (20:00 UTC) in Canada,
 23 the angular radiance field at the shortest wavelengths can be described by a cosine function
 24 expected for conservative scattering in the diffusion domain (King, 1981; King et al.,
 25 1990), where the cloud is expected to have a small to negligible amount of absorption. This

is demonstrated in Fig. 5 (liquid water cloud case), where the angular distribution of the radiation field obtained from measurements (continuous curve, abstracted from Fig. 4a) is compared to that expected in the diffusion domain for conservative scattering (dotted curve) at $\lambda = 0.472 \mu\text{m}$. We note that the angular radiance field becomes increasingly anisotropic as absorption increases in the CAR bands at wavelengths exceeding $1 \mu\text{m}$ (Fig. 4a), because stronger absorption implies that a smaller portion of downwelling solar radiation can be reflected back up from below. In this case, the three conditions for the diffusion domain at a conservative scattering wavelength were met. King et al., (1990) show that when the three conditions are assured, quantitative information about cloud absorption properties from the angular distribution of scattered radiation can be derived, dependent only on the optical properties of the medium and possibly on the reflectivity of the underlying surface, but independent of the solar zenith angle and solar irradiance.

The problem now is to describe the radiation pattern inside an optically thick pyroCu, the core of a pyroCu, and smoke, which seem to be increasingly anisotropic as absorption tends to dominate at the shorter wavelength and is not negligible. However, the diffusion domain theory for optically thick clouds with modified a and b (Eq. 1b; Fig 4b), can also describe the angular radiance distribution in a pyroCu as shown in Fig. 5 (blue solid curve represents measurements, green dotted line represents the fit), but b must assume a negative value, because in this case, the relative radiance is highest at nadir rather than at zenith. The cosine function can also represent the pyroCu core case (Fig. 4c), but an additional $\sin\theta$ term is needed (Eq. 2) to reproduce the bow shaped curves in Figs. 4c and 5 (note that the solid lines represent observations, while dotted lines represent fit to the observations).

$$I(\tau, \cos\theta) = (a + b\cos\theta) + (c + d\sin\theta) \quad (2)$$

which requires only the knowledge of the zenith angle, θ , and some constants. The parameters a and b are easily determined from Eq. 1a & 1b. The last two terms represent a math-

1 mathematical ansatz, where the term c is obtained from zenith and nadir radiances following Eq.
2 1b, and d was determined through trial and error until the best fit was found ($d = -0.1$). It
3 is interesting to see that radiation transport in an optically thick pyroCu core can be de-
4 scribed by simple geometrical functions, whereby the first two terms represent scattering
5 processes, while the third and fourth terms represent absorption processes. To gain better
6 understanding of radiation transport in a pyroCu, we next attempt to reproduce the radiation
7 pattern observed by the CAR instrument using 1D and 3D Monte Carlo simulations.

8 3.2 *Monte Carlo Simulation*

9 We now explore the optical characteristics of pyroCu using 1D and 3D Monte Carlo
10 radiative transfer simulations. The Monte Carlo model is an appropriately modified version
11 of the code used in several earlier studies, including Várnai and Marshak (2001), and was
12 also tested in the Intercomparison of 3D Radiation Codes (I3RC) project (Cahalan et al.,
13 2005). The actual code used in this paper was also tested through comparisons with
14 DISORT (Discrete Ordinates Radiative Transfer) model (Stamnes et al. 1988) runs for ab-
15 sorbing, plane-parallel clouds. To keep simulation uncertainties below 0.5%, each result is
16 based on 4 million photon trajectories in backward Monte Carlo simulations.

17 Because the purpose of these Monte Carlo simulations is to understand the basic be-
18 haviours in Fig. 4 (and not to simulate the exact values observed by CAR), the simulations
19 use a simple setup (Fig. 6). The calculations assume a 2D slab cloud that is infinite in the
20 cross-sun (Y) direction, lies between 1 km and 2 km altitudes, and is 1 km wide ($\Delta Z = \Delta X$
21 $= 1$ km). The extinction coefficient is 100 km^{-1} , so the cloud optical thickness is 100 in
22 both Z and X directions. Because we simulate radiances deep inside the cloud, where
23 multiple scattering minimizes the details of the scattering phase function, we assume the
24 cloud particles have a Henyey-Greenstein phase function with an asymmetry parameter of g
25 $= 0.85$. The solar zenith angle is taken as 30° and the surface albedo as 0.2. For simplicity,

1 no atmospheric effects—Rayleigh scattering or gaseous absorption—are considered.

2 Fig. 7 shows simulation results that can shed light onto the behaviours in Figs. 4a, 4b,
3 and 4c. (At this stage we do not attempt to simulate the complex behaviours in Fig. 4d.)
4 The black dashed line displays a qualitatively similar behaviour to the clean cloud in Fig.
5 4a and shows the general behaviour of 1D radiation calculations, which assume horizon-
6 tally homogeneous and infinite (plane-parallel) clouds. The line illustrates that in 1D cases,
7 the radiance of the highly diffuse radiation deep inside clouds is always greater looking up
8 than looking down regardless of the amount of particle absorption. This is because the con-
9 servation of energy and the lack of light sources below imply that the upwelling flux can
10 never exceed the downwelling flux. This particular simulation was based on a single scat-
11 tering albedo of 0.975, representing stronger absorption than typically occur in liquid water
12 clouds in the visible near-infrared (cf. Fig. 4a), but with a shape typical of what occurs in
13 absorbing liquid water clouds.

14 The other three curves in Fig. 7 are from 3D simulations. Energy conservation re-
15 quires the scene average net radiation to flow downward even in 3D situations. However,
16 this trend can reverse locally inside clouds in 3D situations because large amounts of radi-
17 ation can reach the surface easily in clear areas between clouds and, after reflection from
18 the surface, can enter through the cloud base and create an upwelling flow of radiation in-
19 side the cloud. In addition, sunlight entering through a sunlit cloud side can create a hori-
20 zontal net flow toward the shadowy side (Fig. 6).

21 The blue squares in Fig. 7 show that the downward flow entering through the cloud
22 top still dominates our 3D case if there is no absorption. The red circles, however, show
23 that absorption can drastically change the radiation pattern by depleting much of the
24 downwelling radiation wending its way through the cloud. As a result, the upwelling flow
25 of radiation reflected from the surface can match the weakened downwelling flow, creating

1 comparable intensity peaks looking up ($\theta=0^\circ$) and down ($\theta=180^\circ$). This is similar to the
2 behaviour in Fig. 4c (pyroCu core). Lastly, the green dashed curve in Fig. 7 shows that for
3 a lower altitude cloud absorption reduces the downwelling (upwelling) radiation more
4 (less), and so upwelling radiation can fully dominate and create a trend similar to that in
5 Figure 4b (pyroCu).

6 Finally, Fig. 8 more explicitly explores the role of absorption and scattering proper-
7 ties in shaping radiation patterns. Fig. 8a shows that even relatively weak absorption ($\text{SSA} \leq$
8 0.99) can allow upwelling radiation to match or even exceed the downwelling flow in a 3D
9 situation. In turn, Fig. 8b shows that increasing the number of particles (i.e., the extinction
10 coefficient) yields similar effects to increasing their absorptivity, as both changes make it
11 harder for radiation to reach an instrument deep inside the cloud. This implies that radiation
12 patterns similar to those observed in pyroCu and pyroCu core (Figs. 4b and 4c) can arise in
13 thick clouds even if absorption is relatively weak, although stronger absorption is required
14 in thin clouds. The interplay between scattering and absorption can also allow upwelling
15 radiation to dominate even in the upper parts of clouds if particles are distributed unevenly.
16 For example, if the cloud extinction coefficient increases with altitude (e.g., Raga and
17 Jonas, 1993)—e.g., as ascending droplets grow through condensation—strong absorption or
18 scattering above can greatly reduce the downwelling radiation and allow the upwelling ra-
19 diation reflected from the ground to dominate even at high altitudes.

20 4. Conclusions

21 This study provides an analysis of airborne radiation measurements with the CAR in-
22 strument within strong pyroCu over boreal forest fires in Saskatchewan, Canada during the
23 Arctic Research of the Composition of the Troposphere from Aircraft and Satellites (ARC-
24 TAS) summer field campaign in 2008.

1 We found the pyroCu core to be very interesting having very low light levels from the
2 UV to near IR regions of the electromagnetic spectrum, and very uniform radiance field in
3 all directions. Spectral radiances measured within the core were very small $< 1 \text{ Wm}^{-2}\mu\text{m}^{-1}$
4 sr^{-1} in the ultraviolet and visible bands, $\lambda < 0.5 \mu\text{m}$, and at $\lambda=1.6 \mu\text{m}$, but substantially lar-
5 ger ($2-5 \text{ Wm}^{-2}\mu\text{m}^{-1}\text{sr}^{-1}$) for $0.5 \mu\text{m} < \lambda < 1.3 \mu\text{m}$, independent of direction. We found the
6 angular distribution of radiance within the pyroCu to be related to the diffusion domain in
7 water clouds that can be described by very similar cosine functions with an additional sine
8 term. We demonstrate with Monte Carlo simulation that radiation transport in pyroCu is
9 inherently a 3D problem and must account for strong particle absorption. The proposed
10 simple description of the radiation distribution within the pyroCu or pyroCu core may lead
11 to better understanding of these cloud systems and provide a simpler solution for their in-
12 clusion in climate models. Based on the low radiation values measured in the core of the
13 pyroCu, we speculate that the formation of the dark core is an important feature for estab-
14 lishment of a possible pathway for transportation of fire emissions to the upper troposphere
15 and lower stratosphere, but this remains to be validated.

16 Acknowledgements

17 This research was supported by the Science Mission Directorate of the National
18 Aeronautics and Space Administration as part of the Radiation Sciences Program under Hal
19 B. Maring and Airborne Science Program under Bruce Tagg. We also thank F. Ewald, P.
20 Kundu, R. A. Marshak, W. Wiscombe, A. Nenes, and T. Lathem for insightful discussions
21 and comments. This work was performed under NASA Grants NNX08A89G and
22 NNX11AQ98G.

23 References

24 Barrick, J. D., Aknan, A. A., 2008. P-3B Supporting Measurements Data System (PDS):

- 1 <http://www.espo.nasa.gov/arctas/docs/instruments/pds.pdf>
- 2 Cahalan R.F., Oreopoulos, L., Marshak, A., Evans, K.F., Davis, A., Pincus, R., Yetzer, K.,
3 Mayer, B., Davies, R., Ackerman, T., Barker, H., Clothiaux, E., Ellingson, R., Garay,
4 M., Kassianov, E., Kinne, S., Macke, A., OHirok W., Partain, P., Prigarin, S., Rublev,
5 A., Stephens, G., Szczap, F., Takara, E., Várnai, T., Wen, G., Zhuravleva, T., 2005.
6 The International Intercomparison of 3D Radiation Codes (I3RC): Bringing together
7 the most advanced radiative transfer tools for cloudy atmospheres, Bull. Amer. Meteor.
8 Soc., 86, 1275-1293.
- 9 Clarke, A., McNaughton, C., Kapustin, V., Shinozuka, Y., Howell, S., Dibb, J., Zhou, J.,
10 Anderson, B., Brekhovskikh, V., Turner, H., Pinkerton, M., 2007. Biomass burning
11 and pollution aerosol over North America: Organic components and their influence on
12 spectral optical properties and humidification response, J. Geophys. Res., 112,
13 D12S18, doi:10.1029/2006JD007777.
- 14 Damoah, R., Spichtinger, N., Servranckx, R., Fromm, M., Eloranta, E.W., Razenkov, I.A.,
15 James, P., Shulski, M., Forster, C., Stohl, A., 2006. A case study of pyro-convection
16 using transport model and remote sensing data, Atmos. Chem. Phys., 6, 173–185.
- 17 Fromm, M., Lindsey, D.T., Servranckx, R., Yue, G., Trickl, T., Sica, R., Doucet, P., Godin-
18 Beekmann, S., 2010. The untold story of pyrocumulonimbus, Bull. Ameri. Meteor.
19 Soc., 91, 1193–1209.
- 20 Fromm, M., Bevilacqua, R., Servranckx, R., Rosen, J., Thayer, J., Herman, J., Larko, D.,
21 Servranckx, R., 2005. Pyro-cumulonimbus injection of smoke to the stratosphere: Ob-
22 servations and impact of a super blowup in northwestern Canada on 3–4 August 1998,
23 J. Geophys. Res., 110, D08205, doi:10.1029/2004JD005350.
- 24 Fromm, M., Servranckx, R., 2003. Transport of forest fire smoke above the tropopause by
25 supercell convection, Geophys. Res. Lett., 30, 1542, doi:10.1029/2002GL016820.

- 1 Gatebe, C.K., King, M.D., Platnick, S., Arnold, G.T., Vermote, E.F., Schmid, B., 2003.
2 Airborne spectral measurements of surface-atmosphere anisotropy for several surfaces
3 and ecosystems over southern Africa, *J. Geophys. Res.*, 108, 8489,
4 doi:10.1029/2002JD002397.
- 5 Giglio, L., Descloitres, J., Justice, C., Kaufman, Y., 2003. An enhanced contextual fire de-
6 tention algorithm for MODIS. *Remote Sens. Environ.*, 87, 273–282.
- 7 Howell, S.G., Clarke, A.D., Shinozuka, Y., Kapustin, V., McNaughton, C.S., Huebert, B.J.,
8 Doherty, S.J., Anderson, T.L., 2006. Influence of relative humidity upon pollution and
9 dust during ACE-Asia: Size distributions and implications for optical properties, *J.*
10 *Geophys. Res.* 111, D06205, doi:10.1029/2004JD005759.
- 11 Ichoku, C., Giglio, L., Wooster, M.J., Remer, L.A., 2008. Global characterization of bio-
12 mass-burning patterns using satellite measurements of Fire Radiative Energy, *Remote*
13 *Sens. Environ.*, 112, 2950-2962.
- 14 Jacob, D.J., Crawford, J.H., Maring, H., Clarke, A.D., Dibb, J.E., Emmons, L.K., Ferrare,
15 R.A., Hostetler, C.A., Russell, P.B., Singh, H.B., Thompson, A.M., Shaw, G.E.,
16 McCauley, E., Pederson, J.R., Fisher, J.A., 2010. The Arctic Research of the Compo-
17 sition of the Troposphere from Aircraft and Satellites (ARCTAS) mission: design,
18 execution, and first results. *Atmos. Chem. Phys.*, 10, 5191–5212.
- 19 Kahn, R.A., Chen, Y., Nelson, D.L., Leung, F.Y., Li, Q.B., Diner, D.J., Logan, J.A., 2008.
20 Wildfire smoke injection heights: two perspectives from space, *Geophys. Res. Lett.*,
21 35, L04809, doi:10.1029/2007GL032165.
- 22 King, M.D., Radke, L.F., Hobbs, P.V., 1990. Determination of the spectral absorption of
23 solar radiation by marine stratocumulus clouds from airborne measurements within
24 clouds, *J. Atmos. Sci.*, 47, 894–907.
- 25 King, M.D., Strange, M.G., Leone, P., Blaine, L.R., 1986. Multiwavelength scanning radi-

- 1 ometer for airborne measurements of scattered radiation within clouds, *J. Atmos.*
2 *Oceanic Technol.* 3, 513–522.
- 3 King, M.D., 1981. A method for determining the single scattering albedo of clouds through
4 observation of the internal scattered radiation field, *J. Atmos. Sci.*, 38, 2031–2044.
- 5 Luderer, G., Trentmann, J., Winterrath, T., Textor, C., Herzog, M., Graf, H.-F., Andreae,
6 M.O., 2006. Modeling of biomass smoke injection into the lower stratosphere (part II):
7 sensitivity studies, *Atmos. Chem. Phys.*, 6, 5261–5277.
- 8 McCarter, R.J., Broido, A., 1965. Radiative and convective energy from wood crib fires,
9 *Pyrodyn.*, 2, 65–85.
- 10 Packham, D.R., 1969. Heat transfer above a small ground fire, *Australia Forest Research* 5,
11 19–24.
- 12 Pilewskie, P., Pommier, J., Bergstrom, R., Gore, W., Howard, S., Rabbette, M., Schmid, B.,
13 Hobbs, P.V., Tsay, S.C., 2003. Solar spectral radiative forcing during the Southern Af-
14 rican Regional Science Initiative, *J. Geophys. Res.*, 108, 8486,
15 doi:10.1029/2002JD002411.
- 16 Provencal, R., Gupta, M., Owano, T.G., Baer, D.S., Ricci, K.N., O'Keefe, A., Podolske, J.R.,
17 2005. Cavity-enhanced quantum-cascade laser-based instrument for carbon monoxide
18 measurements, *Appl. Opt.*, 44, 6712–6717.
- 19 Raga, G.B., Jonas, P.R., 1993. Microphysical and radiative properties of small cumulus
20 clouds over the sea, *Quart. J. Royal Meteor. Soc.*, 119, 1399–1417.
- 21 Roberts, G., Nenes, A., 2005. A continuous-flow streamwise thermal-gradient CCN cham-
22 ber for atmospheric measurements, *Aerosol Sci. Technol.*, 39, 206–221.
- 23 Russell, P.B., Livingston, J.M., Hignett, P., Kinne, S., Wong, J., Hobbs, P.V., 1999. Aero-
24 sol-induced radiative flux changes off the United States Mid-Atlantic coast: compari-
25 son of values calculated from sunphotometer and in situ data with those measured by

- 1 airborne pyranometer, *J. Geophys. Res.*, 104, 2289–2307.
- 2 Shinozuka, Y., Redemann, J., Livingston, J.M., Russell, P.B., Clarke, A.D., Howell, S.G.,
3 Freitag, S., O'Neill, N.T., Reid, E.A., Johnson, R., Ramachandran, S., McNaughton, C.
4 S., Kapustin, V.N., Brekhovskikh, V., Holben, B.N., McArthur, L.J.B., 2011. Airborne
5 observation of aerosol optical depth during ARCTAS: vertical profiles, inter-
6 comparison and fine-mode fraction, *Atmos. Chem. Phys.*, 11, 3673–3688.
- 7 Soja, A.J., Tchebakova, N.M., French, N.H.F., Flannigan, M.D., Shugart, H.H., Stocks,
8 B.J., Sukhinin, A.I., Parfenova, E.I., Chapin, F.S., Stackhouse, P.W., 2007. Climate-
9 induced boreal forest change: predictions versus current observations, *Global and*
10 *Planet. Change*, 56, 274–296.
- 11 Stamnes, K., Tsay, S.-C., Wiscombe, W., Jayaweera, K., 1988. Numerically stable algor-
12 ithm for discrete-ordinate-method radiative transfer in multiple scattering and emitting
13 layered media, *Appl. Opt.*, 27, 2502–2509.
- 14 Stocks, B.J., 1995. The extent and impact of forest fires in northern circumpolar countries.
15 In: Levine, J.S. (Ed.), *Global Biomass Burning: Atmospheric, Climatic, and Biospheric*
16 *Implications*, MIT Press, Cambridge, Massachusetts, pp. 197–202.
- 17 Stocks, B.J., Mason, J.A., Todd, J.B., Bosch, E.M., Wotton, B.M., Amiro, B.D., Flannigan,
18 M.D., Hirsch, K.G., Logan, K.A., Martell, D. L., Skinner, W.R., 2003. Large forest
19 fires in Canada, 1959–1997. *J. Geophys. Res.* 108, 8149, doi: 10.1029/2001JD000484.
- 20 Strawa, A.W., Provencal, R., Owano, T., Kirschstetter, T.W., Hallar, G., Williams, M.B.,
21 2007. Aero3X: Fast, accurate measurement of aerosol optical properties for climate
22 and air quality studies, American Geophysical Union, Fall Meeting 2007, abstract
23 #A53G-03 (<http://adsabs.harvard.edu/abs/2007AGUFMA53G..03S>).
- 24 Trentmann, J., Luderer, G., Winterrath, T., Fromm, M., Servranckx, R., Textor, C., Herzog,
25 M., Andreae, M.O., 2006. Modeling of biomass smoke injection into the lower strato-

- 1 sphere by a large forest fire (Part I): reference study, *Atmos. Chem. Phys.*, 6, 5247–
2 5260.
- 3 Val Martin, M., Logan, J.A., Kahn, R.A., Leung, F.-Y., Nelson, D.L., Diner, D.J., 2010.
4 Smoke injection heights from fires in North America: analysis of 5 years of satellite
5 observations, *Atmos. Chem. Phys.*, 10, 1491–1510.
- 6 Varnai, T., Marshak, A., 2001. Statistical analysis of the uncertainties in cloud optical depth
7 retrievals caused by three-dimensional radiative effects, *J. Atmos. Sci.*, 58, 1540–1548.
- 8 Wooster, M.J., 2002. Small-scale experimental testing of fire radiative energy for quantify-
9 ing mass combusted in natural vegetation fires, *Geophys. Res. Lett.*, 29,
10 doi:10.1029/2002GL015487.
- 11 Wooster, M.J., Roberts, G., Perry, G.L. W., Kaufman, Y.J., 2005. Retrieval of biomass
12 combustion rates and totals from fire radiative power observations: FRP derivation and
13 calibration relationships between biomass consumption and fire radiative energy re-
14 lease, *J. Geophys. Res.*, 110, D24311, doi: 10.1029/2005JD006318.
15

1 Table 1

2 Locations and FRP values of fire pixels detected by Aqua-MODIS on 2 July 2008 at 19:35

3 UTC in the vicinity of the measured pyroCu, as indicated in Fig. 1b

Latitude (°N)	Longitude (°W)	Fire Radiative Power (MW)
55.685	105.283	108.273
55.682	105.299	112.081
55.677	105.331	37.455
55.688	105.320	84.818
55.706	105.320	105.710
55.733	105.334	20.674
55.778	105.235	24.367
55.773	105.267	18.737
55.803	105.197	84.151
55.838	105.150	25.296
55.835	105.166	17.619

Table 2

P-3B Aircraft Instrumentation for ARCTAS

Instrument Name	Data Products	Technique	Principal Investigator	Detection limit (Nominal accuracy)
AERO3X	Aerosol optical properties, NO ₂ mixing ratio	Cavity ring-down extinction; Sample rate: 2 sec. (Strawa et al., 2007).	A. Strawa, NASA ARC	Extinction and scattering – 2 σ sensitivity ≈ 0.2 Mm ⁻¹ , Extinction and scattering – 2 σ precision ≈ 0.1 Mm ⁻¹ , NO ₂ mixing ratio – 2 σ sensitivity better than 1 ppb
Ames Airborne Tracking Sunphotometer (AATS)	Aerosol optical depth and extinction, water vapor column and profile	Tracking Sun photometer, 0.354-2.138 μm (Russell et al. 1999)	J. Redemann, BAERI/NASA ARC	Slant OD ~0.002 (± 0.01) Slant WV ~0.0005 to 0.006 gcm ⁻² ($\pm 8\%$)
Broad Band Radiometers (BBR)	Radiation fluxes (solar: 0.2-3.6 μm & IR: 4.5-42 μm)	Radiometer	A. Bucholtz, NRL	Estimated Accuracy: 3–5%
Cloud Absorption Radiometer (CAR)	Radiance, aerosol, cloud & Earth surface properties	Angular (cross-track zenith to nadir) scanning radiometer, 0.340-2.301 μm	C. Gatebe, USRA/NASA GSFC	Radiance absolute accuracy <5%
Continuous-Flow Streamwise Thermal Gradient Cloud Condensation Nuclei	Cloud Condensation Nuclei (CCN)	Supersaturation generated by relative diffusion of water vapour and heat (Roberts and Nenes, 2005)	A. Nenes, Georgia Tech	SS Range: 0.20 – 0.60%, $\pm 0.05\%$

(CCN) Counter (CFSTGC)				
Carbon monoxide By Attenuated Laser Transmis- sion (COBALT)	CO mixing ratio (mole fraction) at a 1-Hz rate based on measured absorp- tion, gas tempera- ture, and pressure using Beer's Law	off-axis integrated cavity output spec- troscopy – TLAS (Provencal et al. 2005)	J. Podolske, NASA/ARC	Precision: 0.2 ppbv (1-s averaging time), uncertainty <1.0%
Hawaii Group for Environmental Aerosol Research (HiGEAR)	aerosols (Aerosol number, size, com- position, volatility, optical properties; Clarke et al., 2007; Shinozuka et al., 2011, Howell et al., 2006)	OPC, PSAP, TDMA, CN counter, ToF-AMS, SP2, nephelometer	A. Clarke, U. Hawaii	See references: Shinozuka et al., (2011).
Project Data Sys- tem (PDS)	base meteorological (P, T, RH) and navigational meas- urements	See reference: Barrick	John Barrick NASA/LaRC	See references: Barrick
Solar Spectral Flux Radiometer (SSFR)	Solar spectral flux	Spectrometer (380- 1700 nm) with nadir and zenith hemispheric collectors	S. Schmidt, U. Colorado	Absolute accuracy 3-5%. Precision 1%

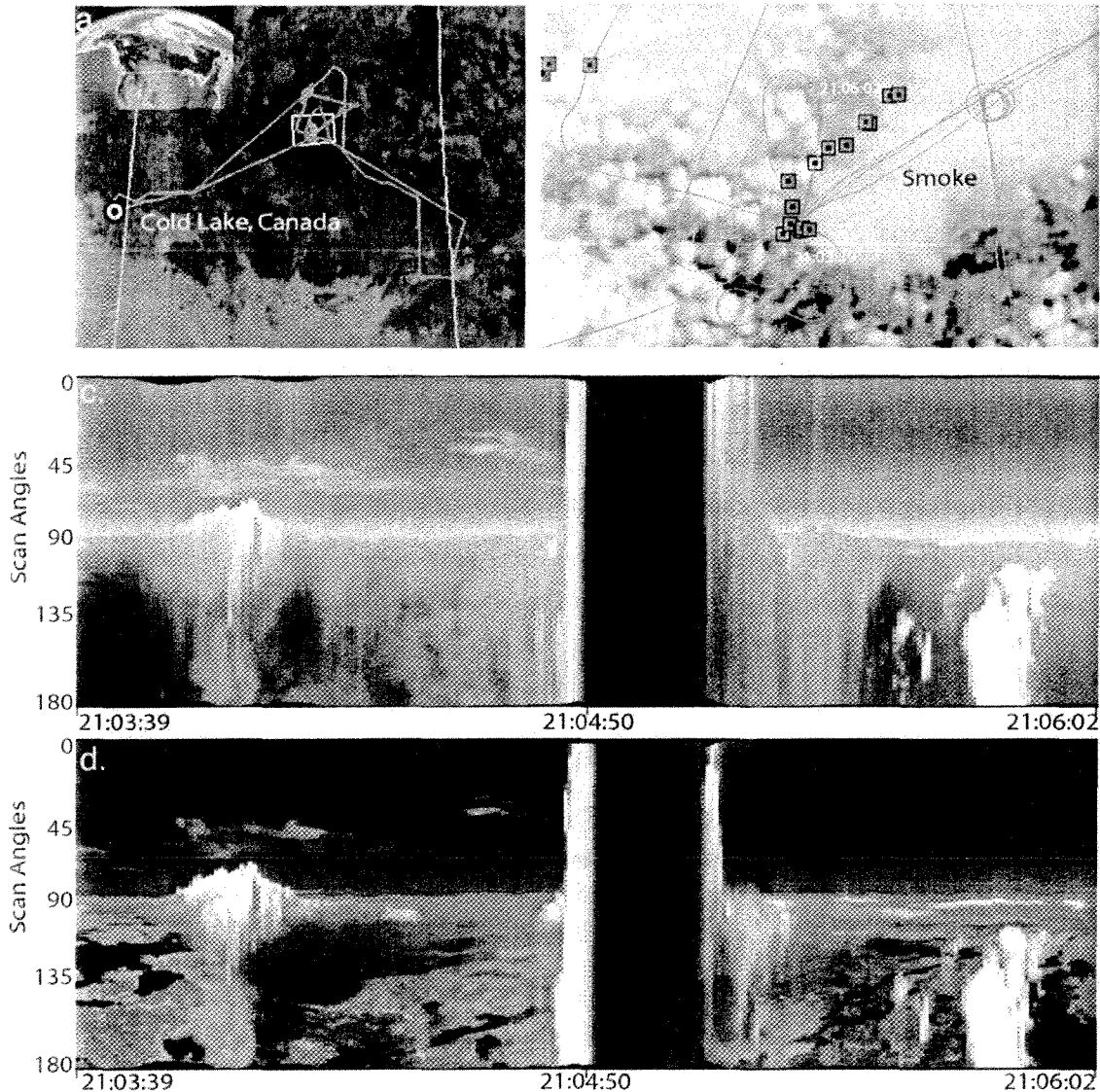


Fig. 1. (a) NASA P-3B flight track 2 July 2008 during the ARCTAS 2008 summer campaign. (b) MODIS/Aqua image taken on 2 July 2008 over the area marked by the rectangle in (a). The red (green) squares are fire locations during Terra (Aqua) overpass at 19:35 UTC (17:55 UTC), and the orange square marks the location of the fire plume that was penetrated by the P-3B. (c)-(d) CAR quick-look images of the fires taken aboard the NASA P-3B over the flight section highlighted in green in (b). A combination of red, green, and blue colors using different CAR bands helps differentiate cloud from smoke, and to see through smoke and identify land surface features such as green vegetation and dark water bodies. The red, green, and blue color assignments in (c) are 0.47, 0.38, 0.34 μm and for (d) 1.66, 1.04, 0.38 μm .

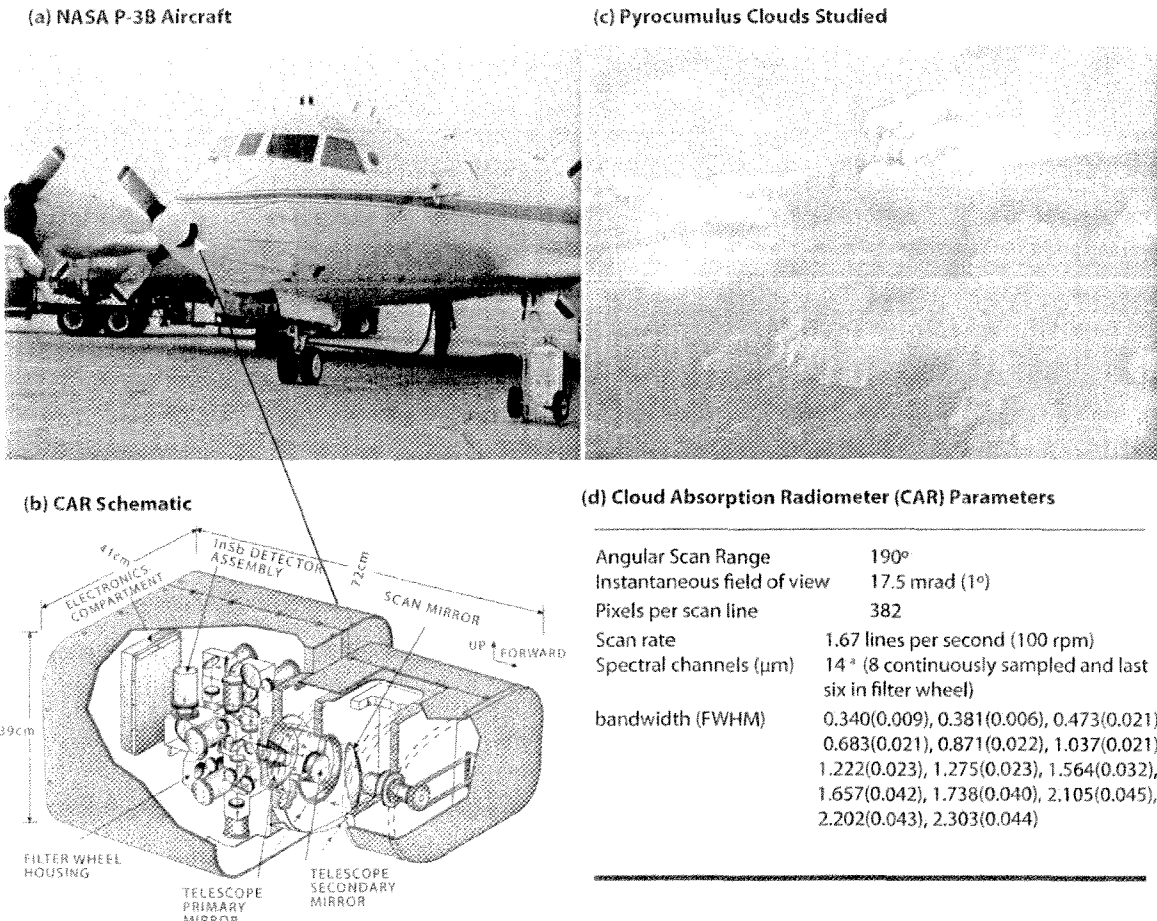
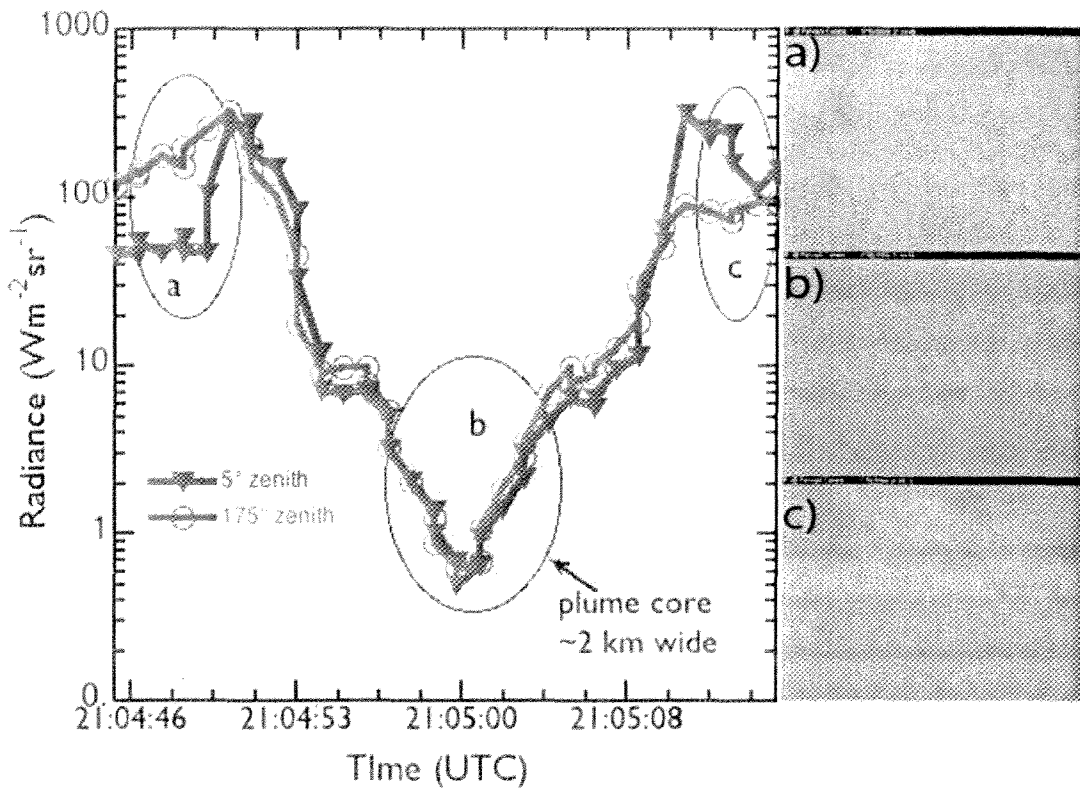


Fig. 2. (a). The NASA P-3B at NASA Ames Research Center, California, USA in June 2008 during the ARCTAS field experiment. (b) Schematic of NASA's Cloud Absorption Radiometer (CAR), which is mounted in the nose of the NASA P-3B aircraft. (c) Picture of the fire plume that the P-3 penetrated on 2 July during ARCTAS. (d) Specifications for the CAR, which contains 14 narrow spectral bands between 0.34 and 2.30 μm . The CAR flew nine fire missions aboard P-3B in Canada between 28 June and 10 July 2008.

Fig. 3. Zenith and nadir radiances at $0.472\text{ }\mu\text{m}$, on a flight through a pyroCu, between 21:04:45 and 21:05:29 UTC, on 02 July 2008. Pictures a, b and c are



from a forward camera aboard the NASA P-3B, and coincide with entry, core penetration, and exit points of the pyroCu, respectively. The core was very dark, and brownish in color. The distance from the core to the edge of the pyroCu is about 318 m (assuming average aircraft speed of 132.5 m/s).

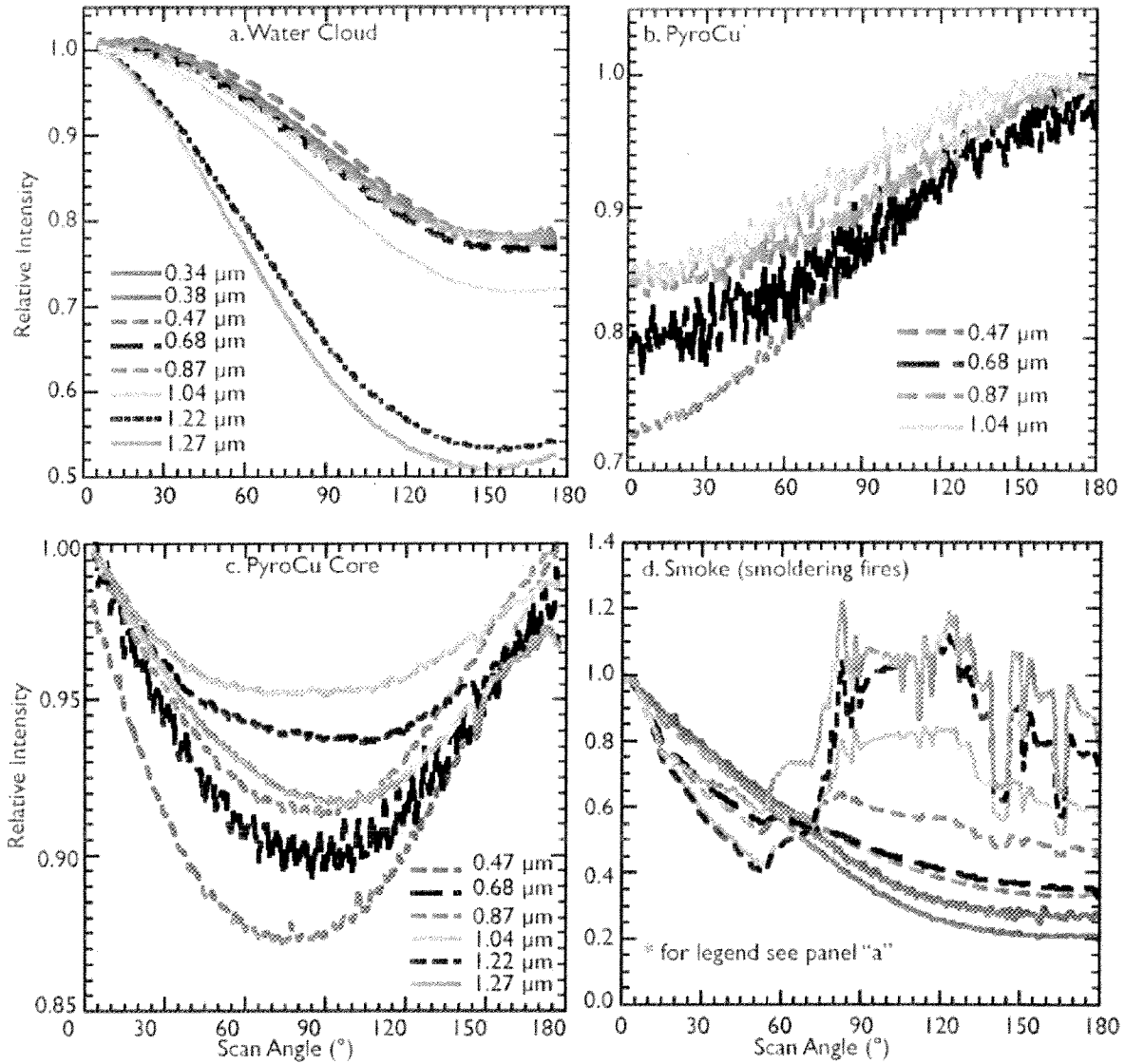


Fig. 4. Relative spectral intensities from CAR as a function of zenith angle for internally scattered radiation measured inside (a) liquid water cloud, (b) pyroCu, (c) core of pyroCu, and (d) thick smoke from smoldering fires with no cloud present. The UV channels are not included in (b) and (c) because of low values of signal-to-noise values. The effects of surface reflectance are clearly seen in the "pure smoke" case (d) at wavelengths, $\lambda \geq 0.68 \mu\text{m}$.

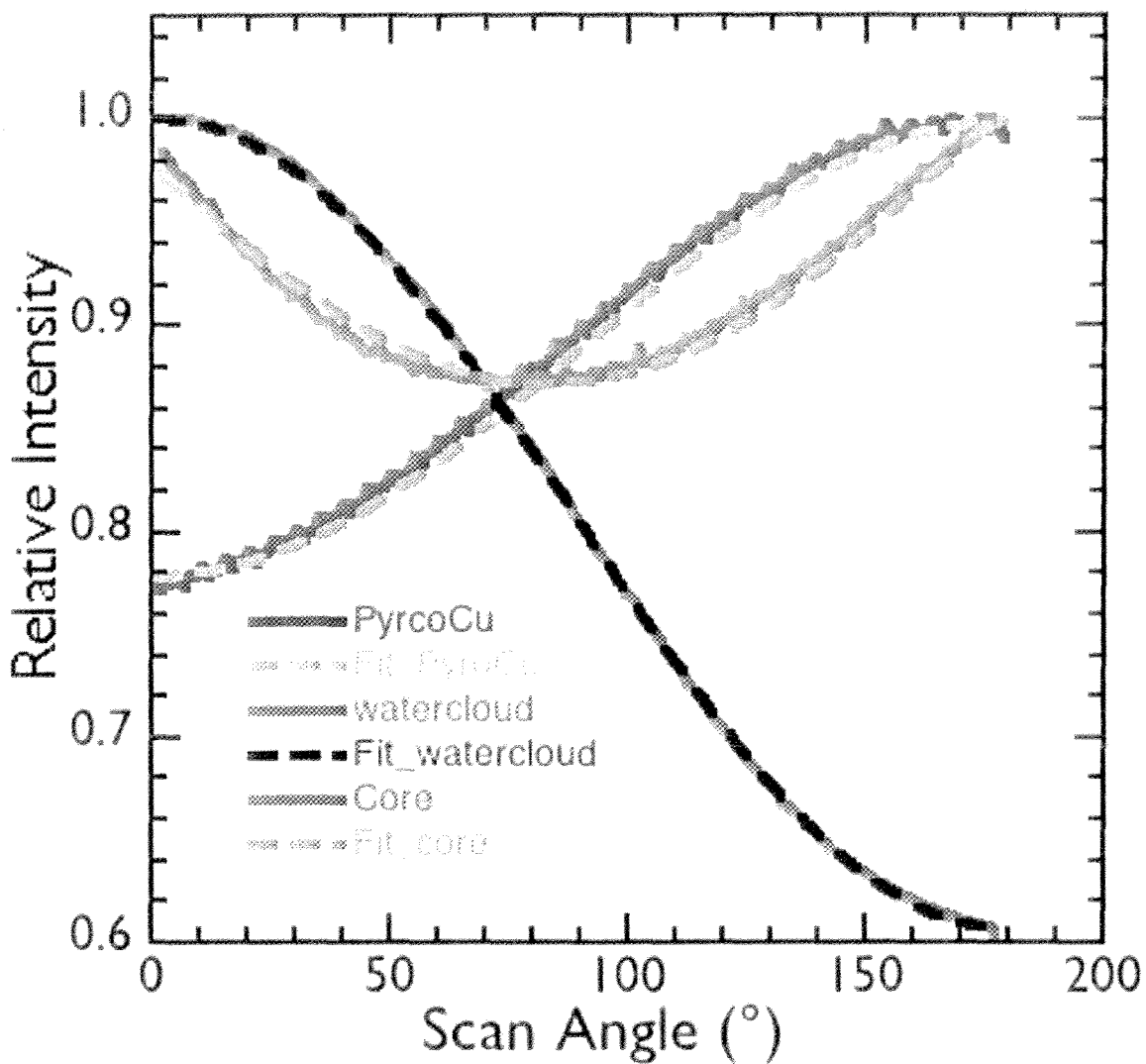


Fig. 5. Observed and fitted relative intensities at $0.472 \mu\text{m}$ represented by solid and dashed lines, respectively, for water cloud, pyroCu and the pyroCu core. The fitted lines for water cloud and pyroCu were generated by a cosine function given in Eq. 1b, with parameter "b" assuming a negative value for the pyroCu case. The pyroCu core was fitted by Eq. 2.

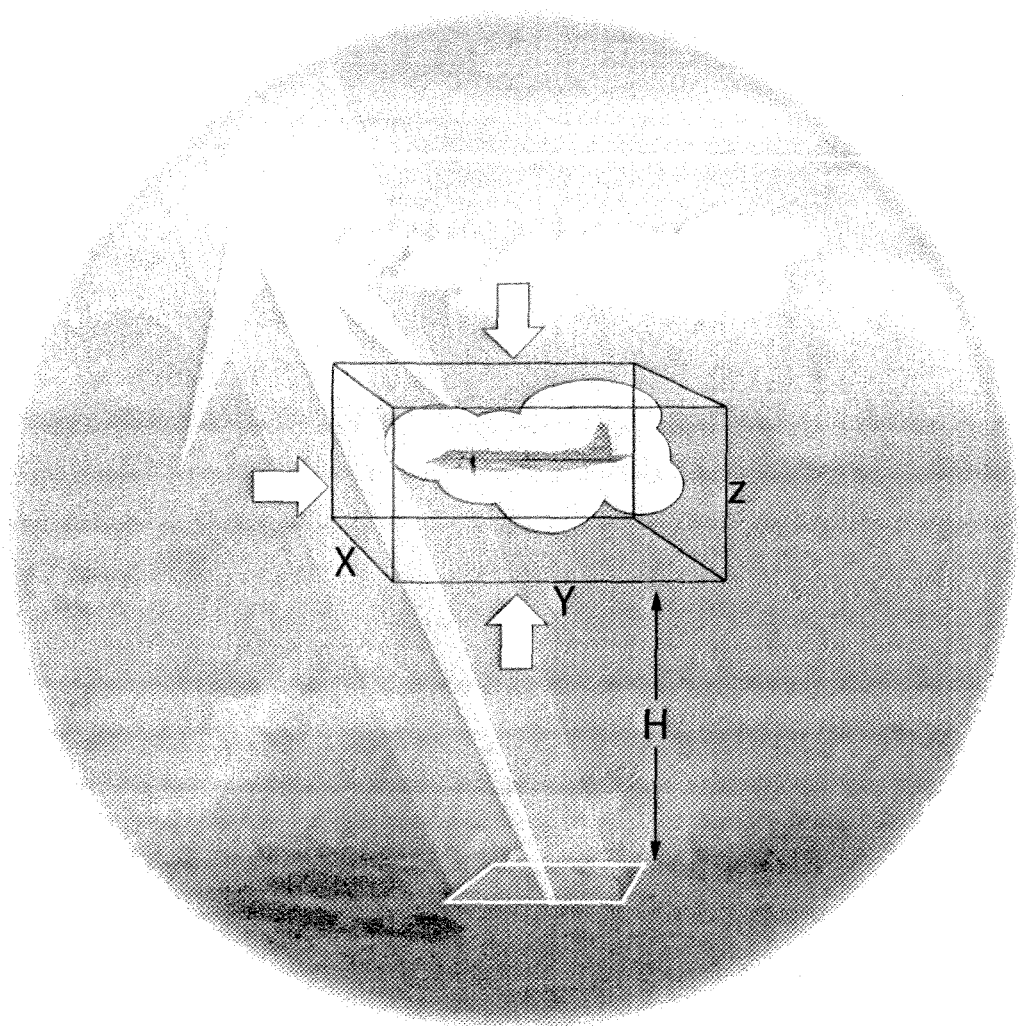


Fig. 6. Illustration of solar illumination paths responsible for the observed radiation patterns in Figs. 4a-c.

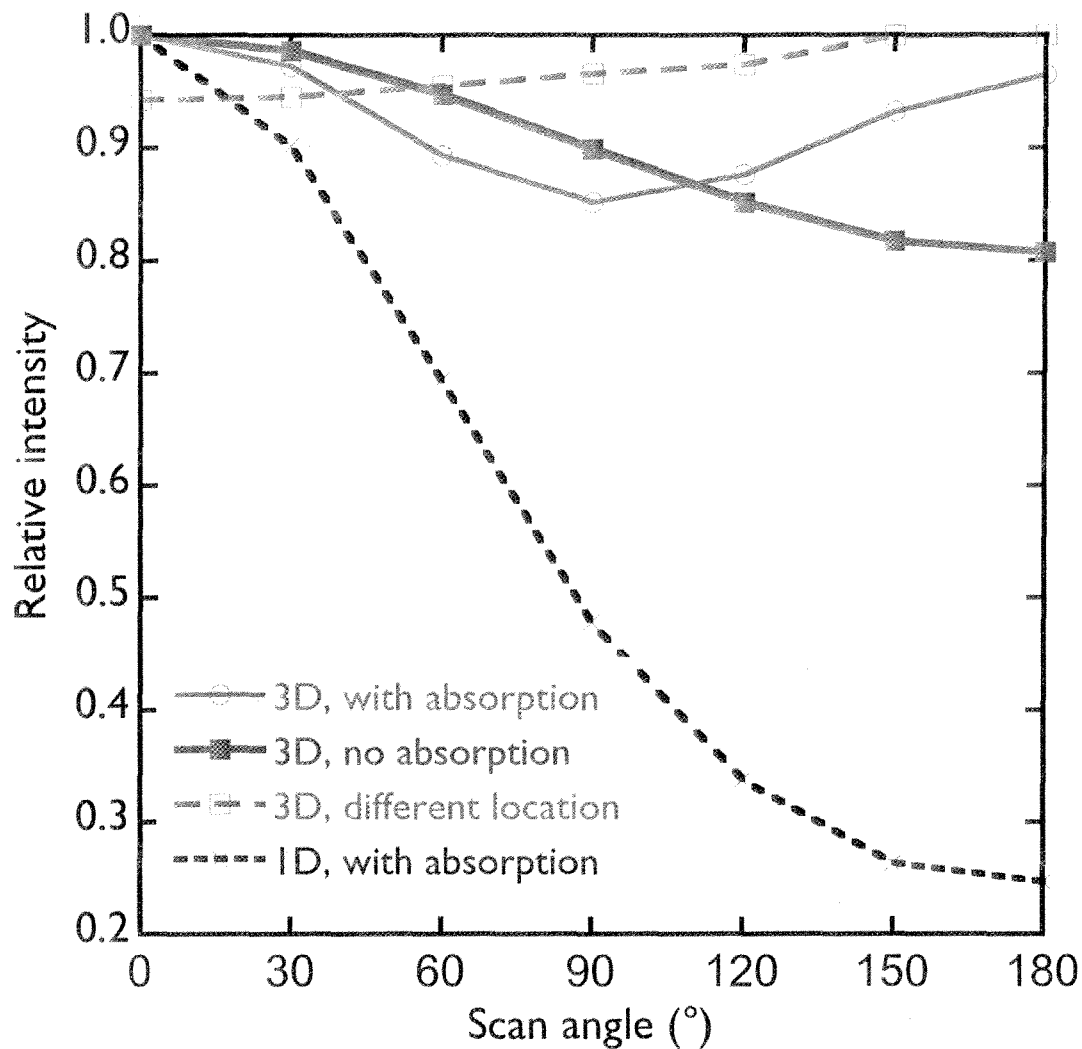


Fig. 7. Simulated CAR data used for understanding the observed behaviors in Fig. 4. The figure shows simulated CAR data for an azimuth perpendicular to the sun (90° relative azimuth). The black, red, and blue curves are for the horizontal center of the cloud at 1.4 km altitude. The green curve, simulating behaviors observed at a different (pyroCu) segment of the flight path, is for a point 200 m away from the sunlit cloud edge at 1.3 km altitude.

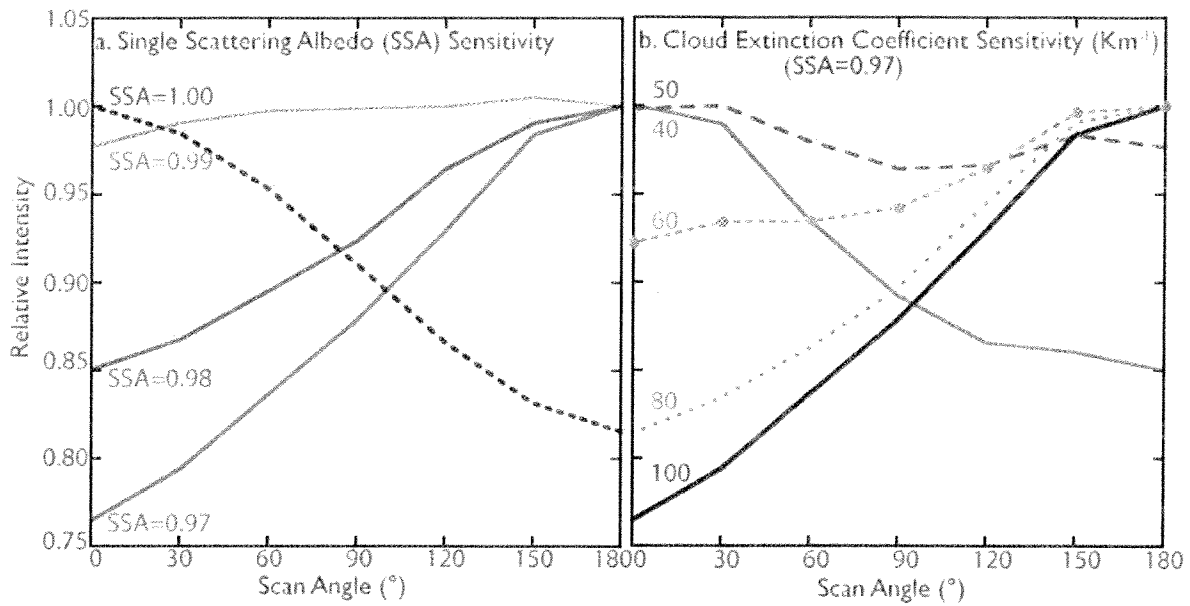


Fig. 8. Impact of (a) variations in single scattering albedo (SSA) at a constant cloud extinction coefficient (100 km^{-1}); and (b) variations in cloud extinction coefficient at a constant SSA (0.97). The simulations are for 85° relative azimuth at a point 300 m away from the sunlit cloud edge at 1.3 km altitude.